Additive Manufacturing 77 (2023) 103822

Contents lists available at ScienceDirect

Additive Manufacturing

journal homepage: www.elsevier.com/locate/addma

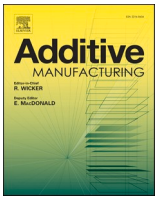

# Voxel-based full-field eigenstrain reconstruction of residual stresses in additive manufacturing parts using height digital image correlation

Fatih Uzun [a,*], Hector Basoalto [b], Konstantinos Liogas [a], Jingwei Chen [a], Igor P. Dolbnya [c], Zifan Ivan Wang [d], Alexander M. Korsunsky [a]

[a] MBLEM, University of Oxford, Department of Engineering Science, Oxford, UK
[b] University of Sheffield, Department of Materials Science and Engineering, Sheffield, UK
[c] Diamond Light Source, B16 Beamline, Didcot, UK
[d] University of Cambridge, Department of Engineering, Cambridge, UK

ARTICLE INFO

*Keywords:*
Eigenstrain reconstruction
Inherent strain
Residual stress
Height digital image correlation
Discontinuous processing

ABSTRACT

The formation of residual stresses is inevitable during the additive manufacturing of metallic parts due to thermo-mechanicals effects, but the chaotic nature of printing processes makes it impossible to have a comprehensive understanding about the magnitude and distribution of these residuals. The voxel-based eigenstrain (inherent strain) reconstruction method is capable of the full-field reconstruction of residual stresses in discontinuous processing bodies at a scale that depends on the resolution of experimental data without using simplifying assumptions and regularisation functions. This advanced method firstly maps the distribution of eigenstrains and then quantifies corresponding residual stresses, residual elastic strains, and displacements by a cost-effective linear elastic computational framework. The reliability of this process solely depends on the quality of experimental data and the availability of computational power. The motivation behind this study is the use of the voxel-based eigenstrain reconstruction method for the full-field mapping of complex residual stress fields, that cannot be predicted by regularizing assumptions, in discontinuous processing additive manufacturing parts. The height Digital Image Correlation (hDIC) technique satisfied the need for high-quality experimental data by calculating triaxial displacements, corresponding to the elastic response of CM 247 LC powder bed fusion (PBF) additive manufacturing part after changes in the boundary conditions due to separation from the base, using optical profilometry measurements at a resolution adjusted in a way to reconstruct Type I residual stresses. Three components of displacements calculated by the hDIC were used to map the distribution of three components of eigenstrains for the reconstruction of six residual stress, six residual elastic strain and three displacement components that belong to the before and after separating from the base states. The reliability of calculations has been validated by monochromatic synchrotron X-ray beams in powder diffraction mode from the same surface of optical profilometry measurements and in transmission mode from the sampling volumes.

## 1. Introduction

Nickel based alloys have been the preferred raw material for the manufacturing of parts at industries such as aerospace [1,2], chemical, nuclear, energy generation [3] because of their creep resistance, strength and toughness at extreme conditions with high temperature and pressure. However, these excellent mechanical properties and high $\gamma'$-phase content [4] create difficulties on the machinability of these materials by conventional subtractive manufacturing techniques [5,6] and necessitates the use of alternative ways of processing like PBF additive manufacturing. The application of this manufacturing technology on the productions of nickel-based super alloy parts has been increasing drastically since the beginning of third millennium [7]. By the use of this technique it has been possible to design and optimise complex forms for specific applications with mesoscale features [8].

CM 247 LC is chemistry the modified version of MAR M 247 superalloy [9] designed for directionally solidified applications to achieve single crystal casting [10]. Although optimised post processing techniques allow improvements in already outstanding mechanical properties and stability of this alloy [11], boundary cracking problems during

* Corresponding author.
*E-mail addresses:* fatihuzun@me.com, fatih.uzun@eng.ox.ac.uk (F. Uzun).

https://doi.org/10.1016/j.addma.2023.103822
Received 21 June 2023; Received in revised form 24 September 2023; Accepted 9 October 2023
Available online 11 October 2023

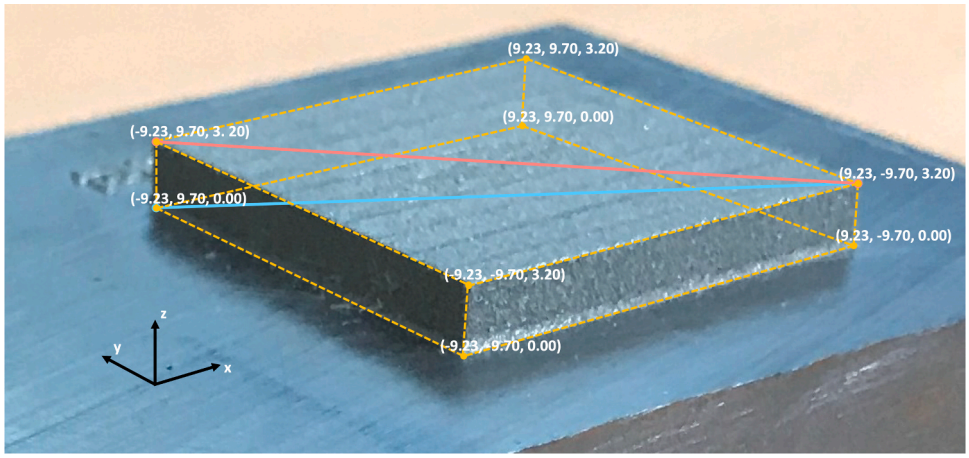


**Fig. 1.** CM 247 LC additive manufacturing part with dimension of 18.46 × 19.40 × 3.20 mm and blue and red diagonal paths located in the model domain.

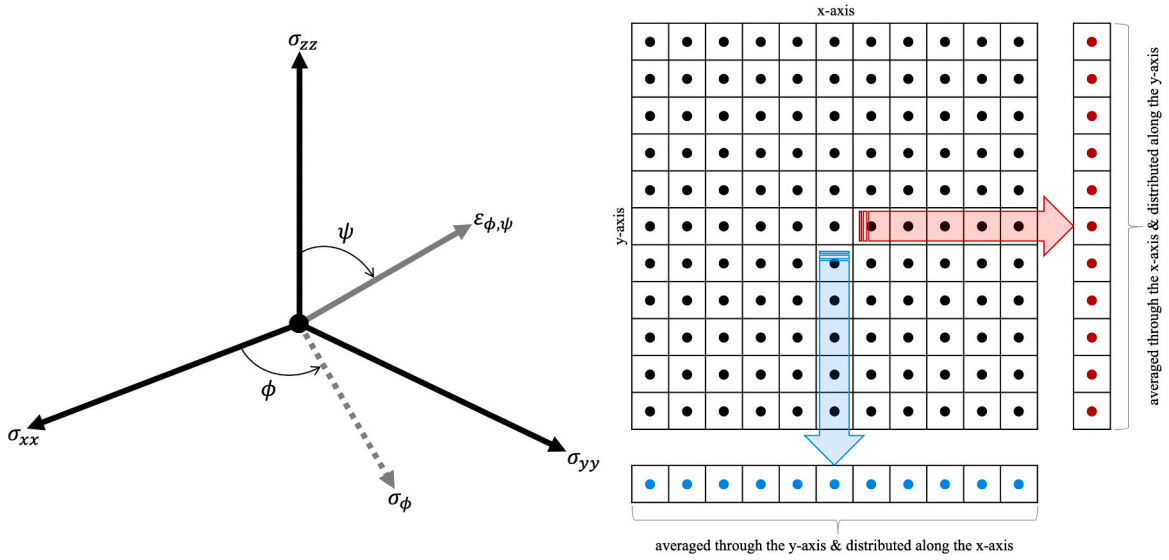


**Fig. 2.** Coordinate system for the calculation of residual stresses where xx- and yy-components are parallel to, and zz-component is normal to the part surface (left). The illustration on the right presents the measurement points along with averaging directions.

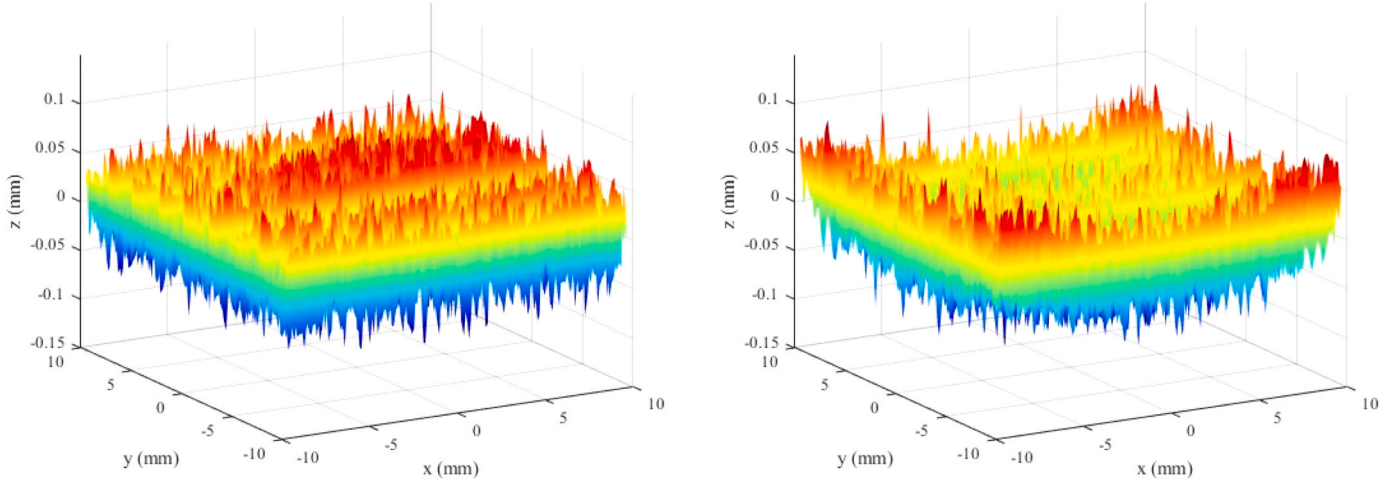


**Fig. 3.** Surface profilometry coordinates belonging to CM 247 LC additive manufacturing part before (left) and after (right) non-contact cutting.

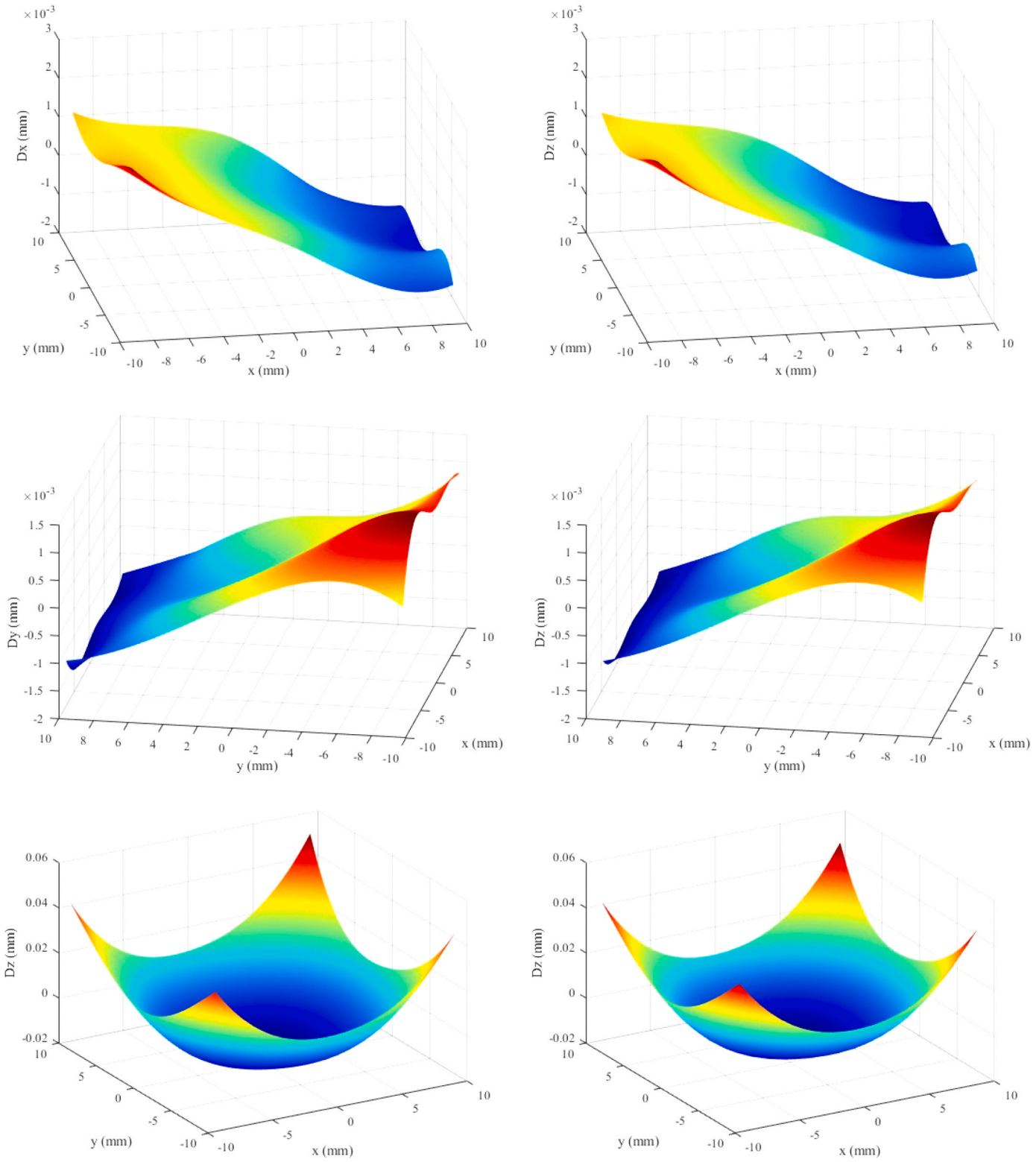


**Fig. 4.** Displacements calculated by the hDIC (left column) and by the voxel-based eigenstrain reconstruction method (right column).

directional solidification [12] and tendency to hot cracking [13] were reported. Weldability of nickel-based alloys can be estimated depending on the γ′-phase volume fraction [14] and alloys with Al and Ti composition, that contribute to γ′-phase formation, higher than 4.5 wt% are stated to have poor weldability [15,16] due to high tendency to crack initiation because of sensitivity to high thermal gradients [17]. Similarly LPFB process leads to rapid heating and cooling cycles that causes nickel alloys with high Al and Ti content to be prone to microcracking [18–20]. Different strategies have been developed to prevent cracking such as fractal scan strategies [17] and pulsed wave laser deposition [21] in CM 247 LC superalloys. Studies on nickel based super alloys that contain high Al and Ti composition also presents techniques to control crack formation by analysing fabrication process parameters [22–26]. Consequently, the reason of cracking behaviour of such alloys can be

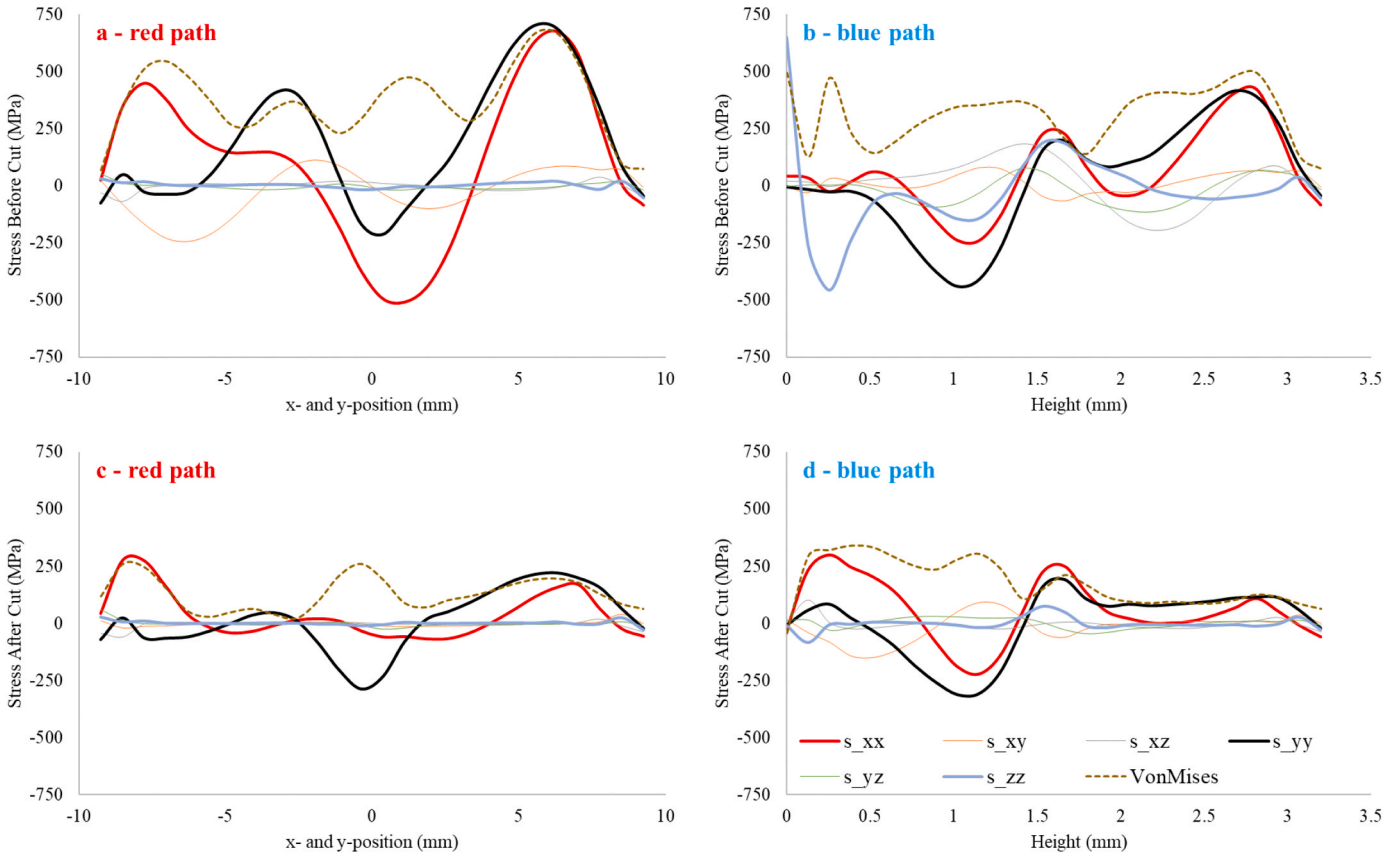


**Fig. 5.** Line plots of six stress components, that distribute along the red and blue paths illustrated in Fig. 1, belonging to before and after the non-contact cutting states.

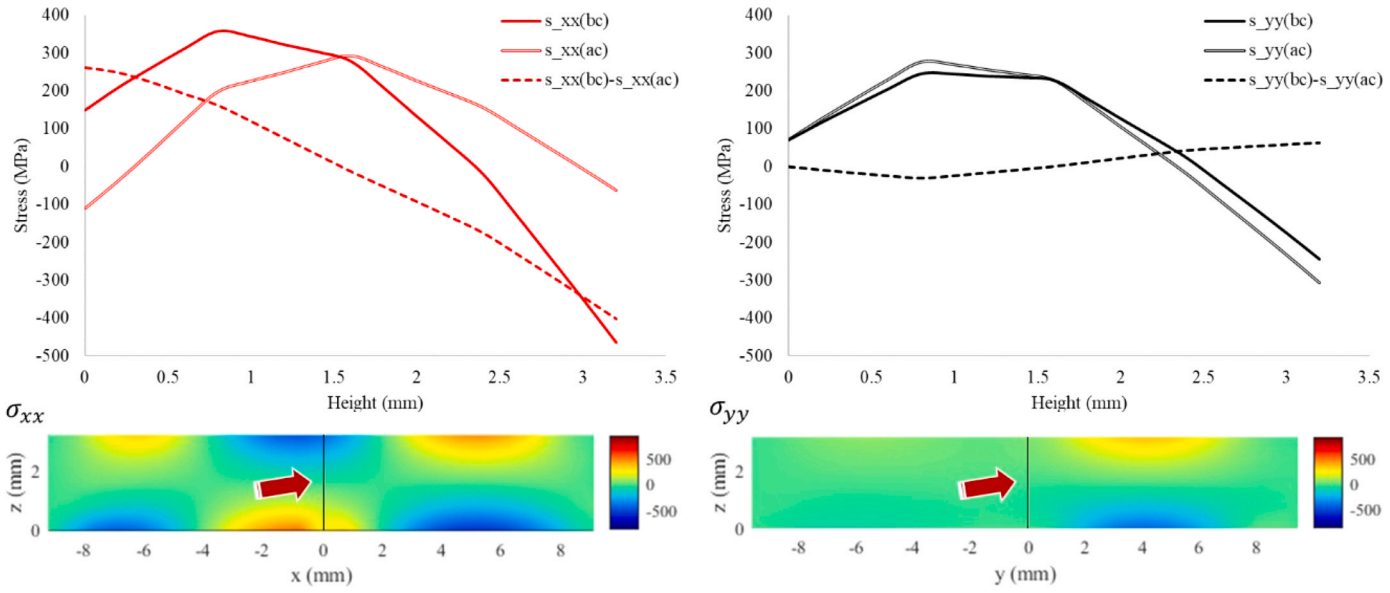


**Fig. 6.** Contour plots of xx- and yy-components of residual stress in the planes that are located at the origin and parallel to x- and y-axes respectively along with line plots that distribute along the z-axis starting from the origin.

stated to be residual stresses formed because of complex thermal history during the manufacturing. The movement of thermal gradients formed by high energy laser beam causes inhomogeneous rapid heating and cooling cycles that results in complex residual stress fields withing the bodies produced by PBF processes. The minimisation of microcrack density or eliminating the formation of mesoscale cracks can only be achieved by minimising the magnitude of residual stresses left within the body because in the case of availability of high magnitude residual stresses the body will be prone to cracking even after the manufacturing. However, the analysis of residual stress fields is a real challenge especially in the case of chaotic processing conditions of lased based additive manufacturing techniques.

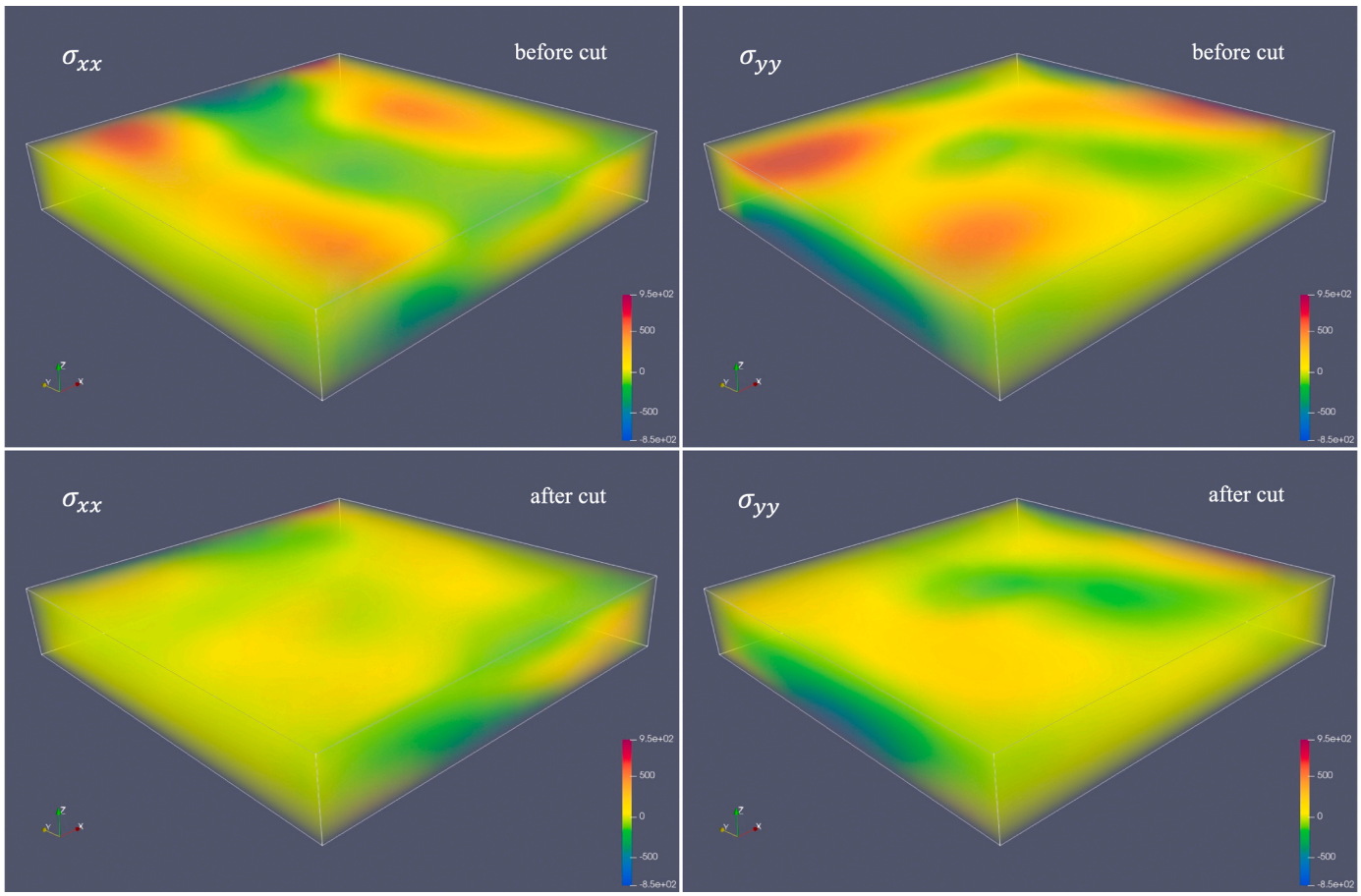


**Fig. 7.** The transparent three-dimensional view of distribution of xx- and yy-components of residual stresses at before and after separation (cut) from the base states.

The quantification of residual stress fields can be achieved by correlating the measurements of destructive or non-destructive experiments with stress magnitude according to mechanical elasticity or by solving elastic-plastic numerical models that simulate the manufacturing process. Destructive techniques rely on measurement of elastic response of the material corresponding to unrecoverable processes like hole drilling [27], surface stripping [28], crack compliance [29] and non-contact cutting [30–35]. On the other hand, non-destructive techniques aim measuring physical properties such as lattice spacing [36–38], velocity of elastic waves [39,40] and Raman effect [41] corresponding to the magnitude of elastic impacts. FIB-DIC technique [42–44] that meets ring cores drilled by focused ion beam [45] with digital image correlation of scanning electron microscopy images can be represented as a semi-destructive technique. Destructive, and non-destructive techniques provide information about residual stresses or residual elastic strains within a limited region of the parts. However, all these techniques are feasible on the mapping strain state within a limited region on the outer surface of parts. Full-field mapping can be possible by neutron diffraction technique [46–51], but the low density of measurement points because of high labour and energy cost makes this technique unfeasible. Accordingly, current experimental techniques are preferred to be used to determine hot spots of residual stress fields. Thermal-structural coupled numerical models also helps understanding the full-field distribution of stress fields [52–55]. These models are based on continuum mechanics for solving partial differential equations in a domain divided into elements. Although calculations of these models can be improved by calibrating model parameters using thermal history measurements, results only provide a rough estimation about the distribution of residual stresses. Different than experimental techniques, numerical models also provide information about the distribution of plastic strains within the domain.

The eigenstrain theory provides an alternative for the determination of distribution of both residual stresses and permanent plastic strains corresponding to a set of experimental data from destructive or non-destructive sources. The use of pre-determined distribution and magnitude of permanent plastic strains for the calculation of corresponding deformations and residual stresses dates back to 1987 [56]. This process is called as reconstruction [57] and the reliability of the calculations depends on the quality of experimental data and the numerical approaches used to create the link between experimental data and permanent plastic strains. In the case of eigenstrain theory, reconstruction is achieved using experimentally determined elastic deformations and accordingly eigenstrain is defined as the permanent plastic strain that are responsible for the measured deformation. The use of profilometry data [58,59] increased the abundance of experimental data used for this process and allowed eigenstrain reconstruction of residual stresses based on simplifying assumptions. Although the reconstructed residual stress fields show a great match with the measurements of diffraction techniques, the distribution of corresponding eigenstrains was dubious until the development of new numerical approaches [58] and principles of artificial intelligence [60–62] for the creation of the link between experimental data and eigenstrain fields for the purpose of understanding the real source of welding residual stress. These achievements allowed the determination of full-field residual stress distribution as a result of complex thermally induced processes, but the proposed numerical techniques rely on simplifying assumptions and regularisation functions [63]. In the case of welding process, it is obvious that eigenstrains must be collected in the vicinity of heat affected zone but in the case of PBF additive manufacturing process the whole printed body is under the influence of high magnitude thermal

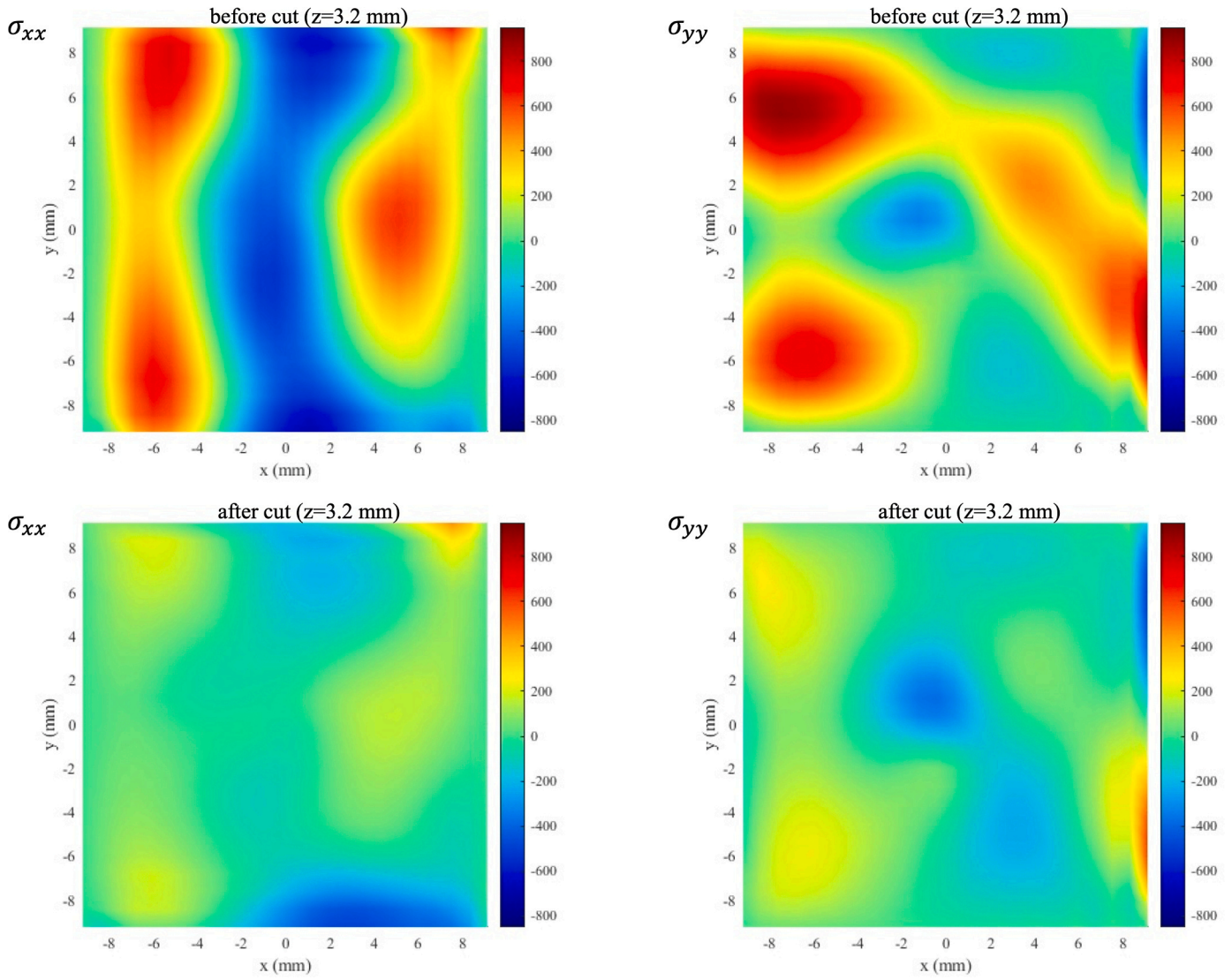


**Fig. 8.** The contour plot of distribution of xx- and yy-components of residual stresses within the top plane for before and after separation (cut) from the base states.

cycles that result in highly complex distribution of eigenstrains that is impossible to predict for defining simplifying assumptions and formulating regularisation functions. Accordingly, for the eigenstrain reconstruction of residual stresses in PBF additive manufacturing parts, it is compulsory to formulate the link between experimental data and eigenstrain fields without relying on simplifying assumptions and regularisation functions. The voxel-based full-field eigenstrain reconstruction method introduced by Uzun and Korsunsky in 2023 [64] satisfies this requirement by creating the link between experimental data and eigenstrain fields solely using radial basis functions that are distributed in a voxel grid. According to the numerical experiments presented in that study, highly reliable full-scale reconstruction of residual stresses is possible with negligible deviation from the reference state. However, these achievements are valid in the case of perfect experimental data of numerical experiments. In order to achieve such accuracy, collection of high quality of experimental data is compulsory.

Digital image correlation have been used for the determination of elastic deformations for the purpose of calculation of corresponding residual stresses [65–67]. However, the correlation of digital images provides only information about planar deviations of surface properties from the reference state. Three dimensional digital image correlation is possible but it provides either very low resolution that is not useful for measuring micro-scale [68–70] displacements or limited to very high resolutions at nano-scale [71–73]. The hDIC developed by Uzun and Korsunsky [74,75] provided a novel approach to the correlation between two states of a material using optical profilometry data [76] for the determination of three axial displacements. This approach allows the quantification of displacements in macro-, meso-, micro- and nano-scales depending on the resolution of profilometry data. Applications of this technique for the determination of displacements and corresponding residual elastic strains in the case of in situ tensile test [74] and operando three point bending [77] presents good match with the other residual stress quantification techniques and satisfy the reliability of the hDIC.

In this study, a novel approach was developed to determine the full-field distribution of six residual stress components along with six residual elastic strain, three eigenstrain and three displacement components in CM 247 LC additive manufacturing part. The approach involved tracking the elastic response of the printed body, after non-contact cutting by electric discharge machine (EDM) from the boundary between the base and print, in terms of three axial displacements, using the hDIC. The availability of rich data and a well-designed algorithm allowed the full-field mapping of the eigenstrain field corresponding to the elastic response. The eigenstrain field was then used to calculate the residual stresses after different processing conditions, that cause changes in the boundary conditions, using a linear elastic finite element

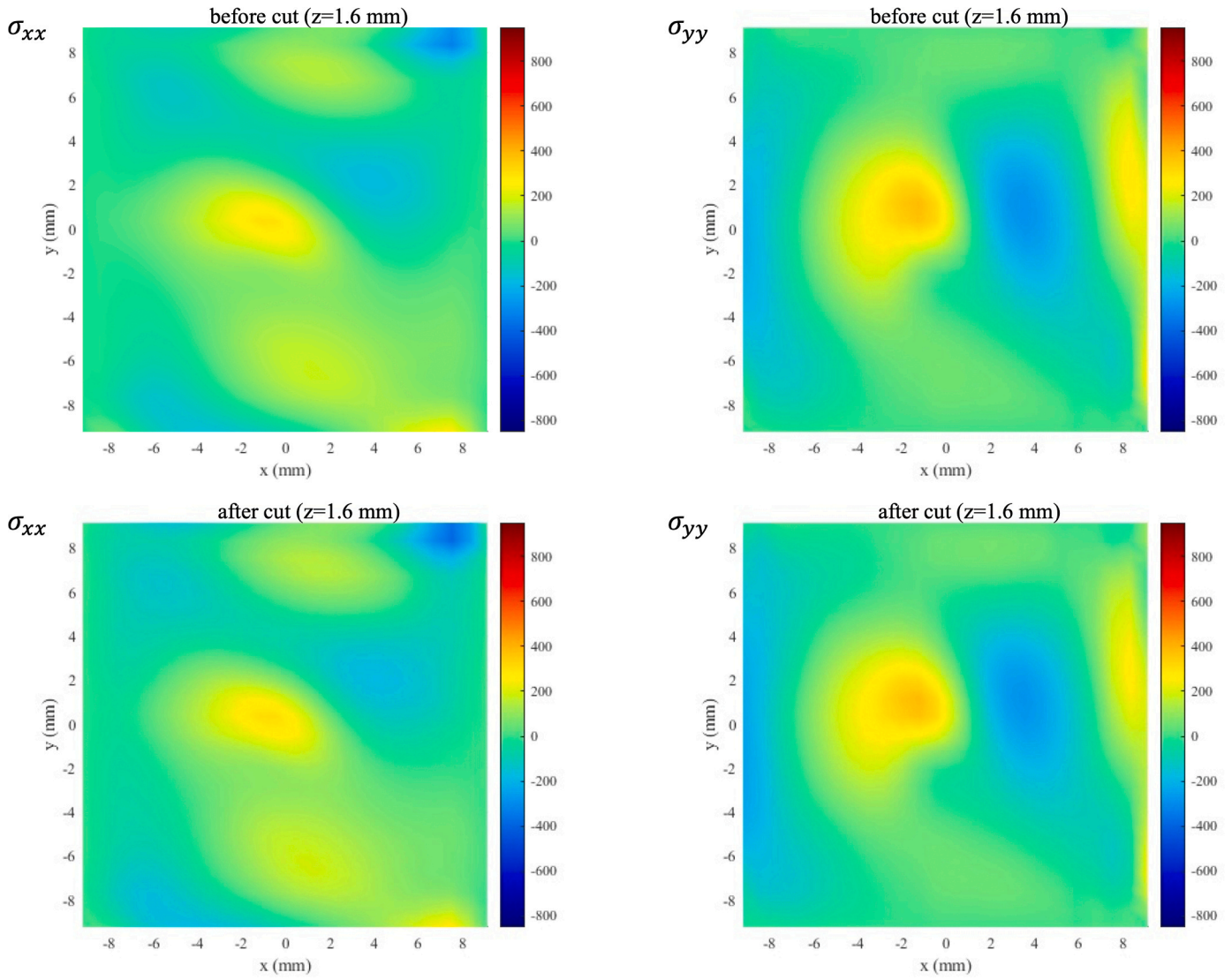


**Fig. 9.** The contour plot of distribution of xx- and yy-components of residual stresses within the middle plane for before and after separation (cut) from the base states.

model. The eigenstrain field determined for the after non-contact cutting state of the printed body was used to calculate the residual stresses before non-contact cutting state and validated by highly reliable X-ray diffraction residual stress quantifications. Additional validation was achieved by obtaining displacements that have perfect match with hDIC correlations. The results of this study showed that the voxel-based eigenstrain reconstruction method is a promising technique for mapping the full-field distribution of residual stresses in additive manufacturing parts.

## 2. Methodology

The voxel-based eigenstrain reconstruction method allows mapping the full-field distribution of residual stresses by creating a link between experimental data and eigenstrain fields using radial basis functions without the requirement of simplifying assumptions and regularisation functions. The only requirement of this modelling approach is rich experimental data. Digital image correlation (DIC), a well-established technique for measuring the displacement of points on a surface using digital images, has the potential to satisfy data requirement. The hDIC is a variant of DIC that has been shown to be capable of determining three axial displacements with high accuracy. In this study, eigenstrain reconstruction of residual stresses was performed using three components of displacements determined by the hDIC using the optical profilometry measurements of Alicona InfiniteFocus microscope that is a high-resolution optical microscope and capable of investigating inter- and intra-granular deformations. Measurements were conducted using this microscope, achieving a resolution of 100 μm in-plane and 1 μm out-of-plane, aligning with the goal of determining Type I stresses.

The additive manufacturing part illustrated in Fig. 1 was first scanned using X-ray diffraction beams to quantify residual stresses for validation of model calculations. The scanning was conducted prior to the separation of the part from the base by non-contact cutting using EDM. Optical profilometry measurements were performed on the top surface of the printed part before and after the separation from the base. The data collected from optical profilometry measurements were used to quantify three components of displacements using the hDIC and to reconstruct three components of eigenstrains, six components of residual elastic strains along with corresponding residual stresses, and three components of displacements using the voxel-based eigenstrain reconstruction method. Additionally, the match of the hDIC displacements with reconstructed displacements provided an additional layer of validation.

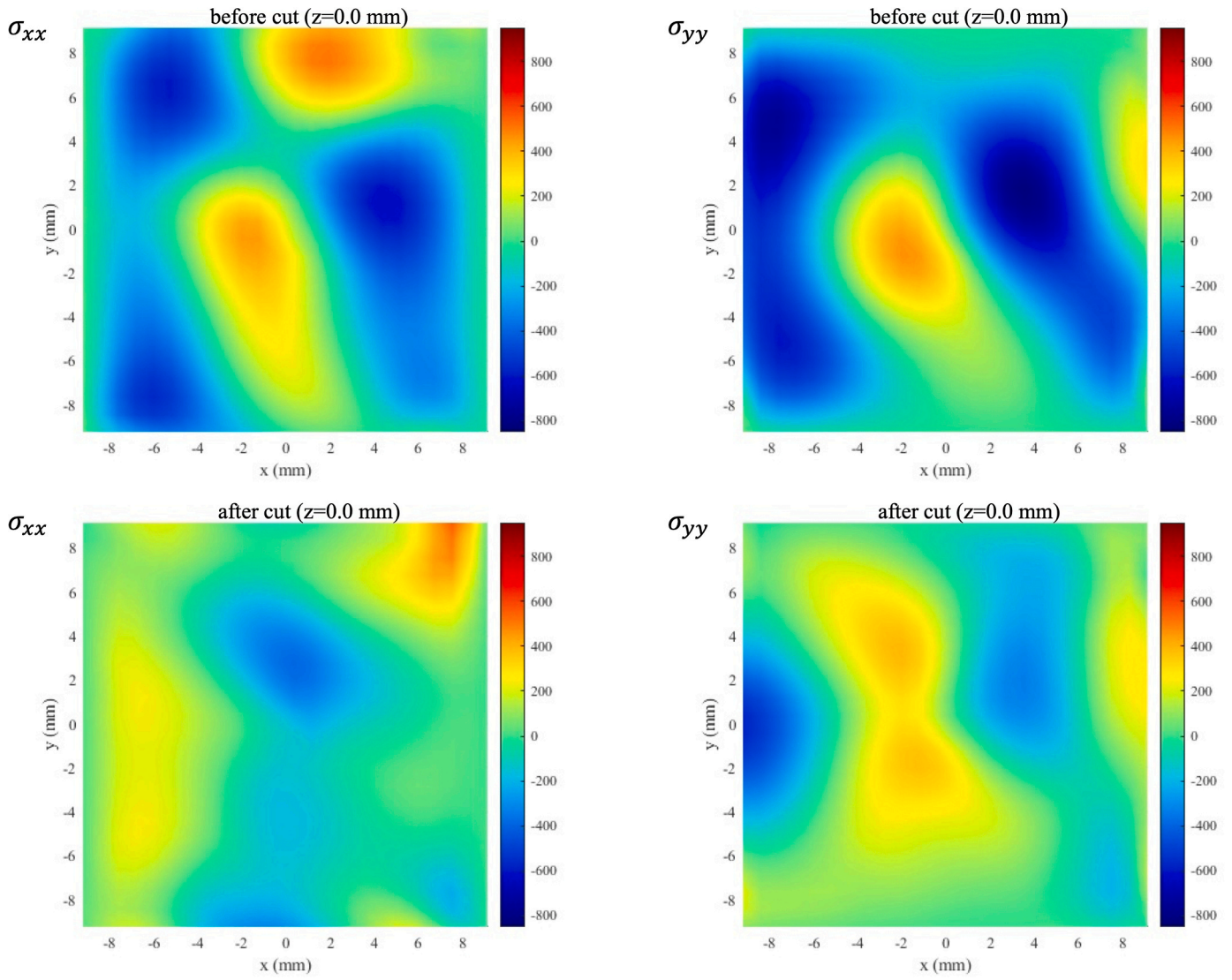


**Fig. 10.** The contour plot of distribution of xx- and yy-components of residual stresses within the bottom plane for before and after separation (cut) from the base states.

### 2.1. Sample preparation

This study presents the use of rich experimental data obtained using the hDIC for the full-field eigenstrain reconstruction of residual stresses in a part with unpredictable residual stress state. This type of parts prevents the use of simplifying assumptions and the derivation of regularization functions. To this end, a CM 247 LC part was prepared using powder bed fusion PBF additive manufacturing technique that creates chaotic thermal effects at the nano- and micro-scales and results in a highly complex and unpredictable residual stress state. This manufacturing was performed without using planned process parameters that could allow having predictions about the distribution of residual stresses. The blind state between specimen design and reconstruction process satisfied by performing these two stages of this project in separate labs located in The University of Sheffield and The University of Oxford respectively. The dimensions of the printed rectangular part are given in Fig. 1 and the origin of the Cartesian coordinates is placed in the middle of the bottom plane of the part.

### 2.2. hDIC

The Alicona InfiniteFocus microscope is able to measure surface profilometry with micron-level in-plane and nanoscale out-of-plane resolution. The hDIC is capable of correlating this optical surface profilometry information, which provides three axial cartesian coordinate information, in contrast to the two-axial distribution of image intensity used in conventional DIC. This property of the hDIC allows the determination of the complete displacement vector of planar surfaces. The correlation is accomplished in two steps that are integer-pixel level cross-correlation and sub-pixel level correlation. Two step correlation process makes it possible to determine large discontinuous displacements due to cracks [75]. The ability to determine large displacements plays an important role because the removal of the printed body from the base is accomplished in operando conditions of the optical profilometry measurement. The profilometry measurements were performed in operando conditions by aligning the sample position using the mechanical fixtures on the base of the optical microscope and by moving the centre of the x-, y-, and z-coordinates to the centre of the Cartesian coordinate system.

The integer-pixel cross-correlation stage of the hDIC correlates pixel subsets with dimension of $(2N+1) \times (2N+1)$, where N represents an integer value that defines the size of the subset, using the zero-mean normalised cross-correlation technique [78]. After the determination of coordinates of matching pixels in the target plane, gradient descent

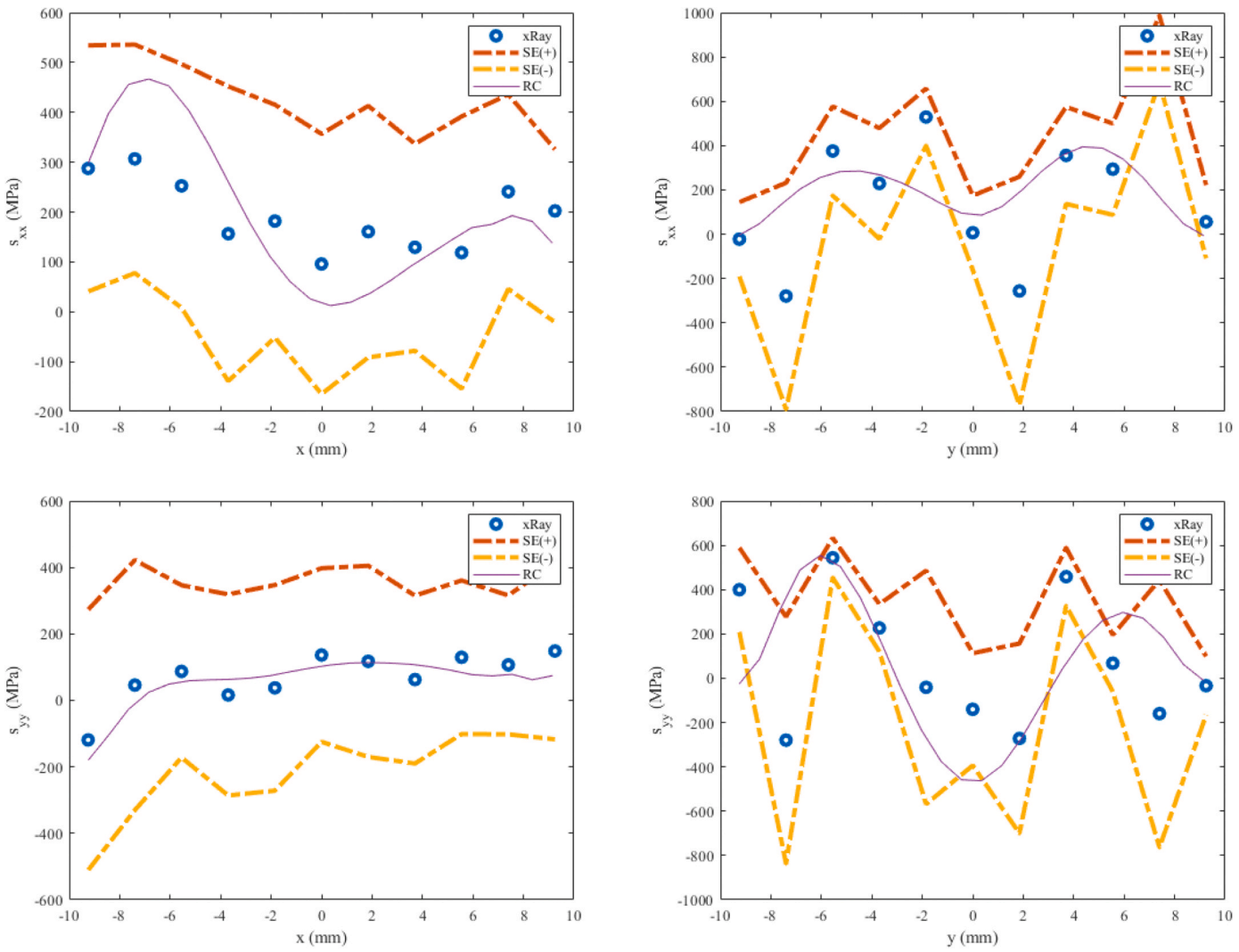


**Fig. 11.** The comparison of residual stresses quantified by the X-ray diffraction $\sin^2\psi$ technique and reconstructed by the voxel-based full-field eigenstrain reconstruction method.

based sub-pixel level correlation is performed to determine matching coordinate in the target plane starting from the target plane coordinates determined during the integer-pixel level cross-correlation. Detailed explanation of the hDIC correlation steps can be found in the study of Uzun and Korsunsky [74] that was published by the International Journal of Mechanical Sciences in 2019. The same correlation procedure explained in that paper was used for the correlation of profilometry data corresponding to the two states of the CM 247 LC additive manufacturing part.

### 2.3. Eigenstrain theory

Eigenstrain theory defines eigenstrains as permanent plastic strains that distribute irregularly in a way to cause formation of residual elastic strain fields. According to this theory, the calculation of residual stresses is possible using eigenstrain fields determined by solving the inverse problem of eigenstrain based on the principle of superposition [58]. In the case of calculation of Type I residual stresses, elastic deformations in a material can be measured using destructively or non-destructively for creating a relation between the measured deformations and independent solutions of basis functions. In this study, all the same formulation of solution to the inverse problem of eigenstrain given in the premier study of Uzun and Korsunsky [64] was used for the calculation of three components of eigenstrain and six components of residual stress along with three components of displacements from three components of experimental data. Weights of independent solutions of the modified radial basis function were calculated without introducing any parameters that influence the distribution. As the model aims to capture all complexities in the distribution of eigenstrains solely based on the resolution of the voxel domain and the distribution and magnitudes are not guided or modified by any supporting function depending on the decisions of the user, this approach does not involve any regularization. Smoothing appears depending on the voxel density of the domain, but this aspect of radial basis functions is out of the scope of this study.

The Voxel-based Eigenstrain reconstruction method enables the mapping of all eigenstrain components using a limited set of experimental data components. The accuracy of the eigenstrain distribution is highest for components that match the experimental data components. Therefore, in this study, only the matching eigenstrain components were mapped to quantify residual stresses using rich experimental data that accommodate information about triaxial displacements corresponding to the elastic response of the printed body as a consequence of the removal from the base.

### 2.4. X-ray diffraction

The interaction between X-ray beams and spacing between atomic planes in a crystal lattice, determined based on the Bragg's Law [79],

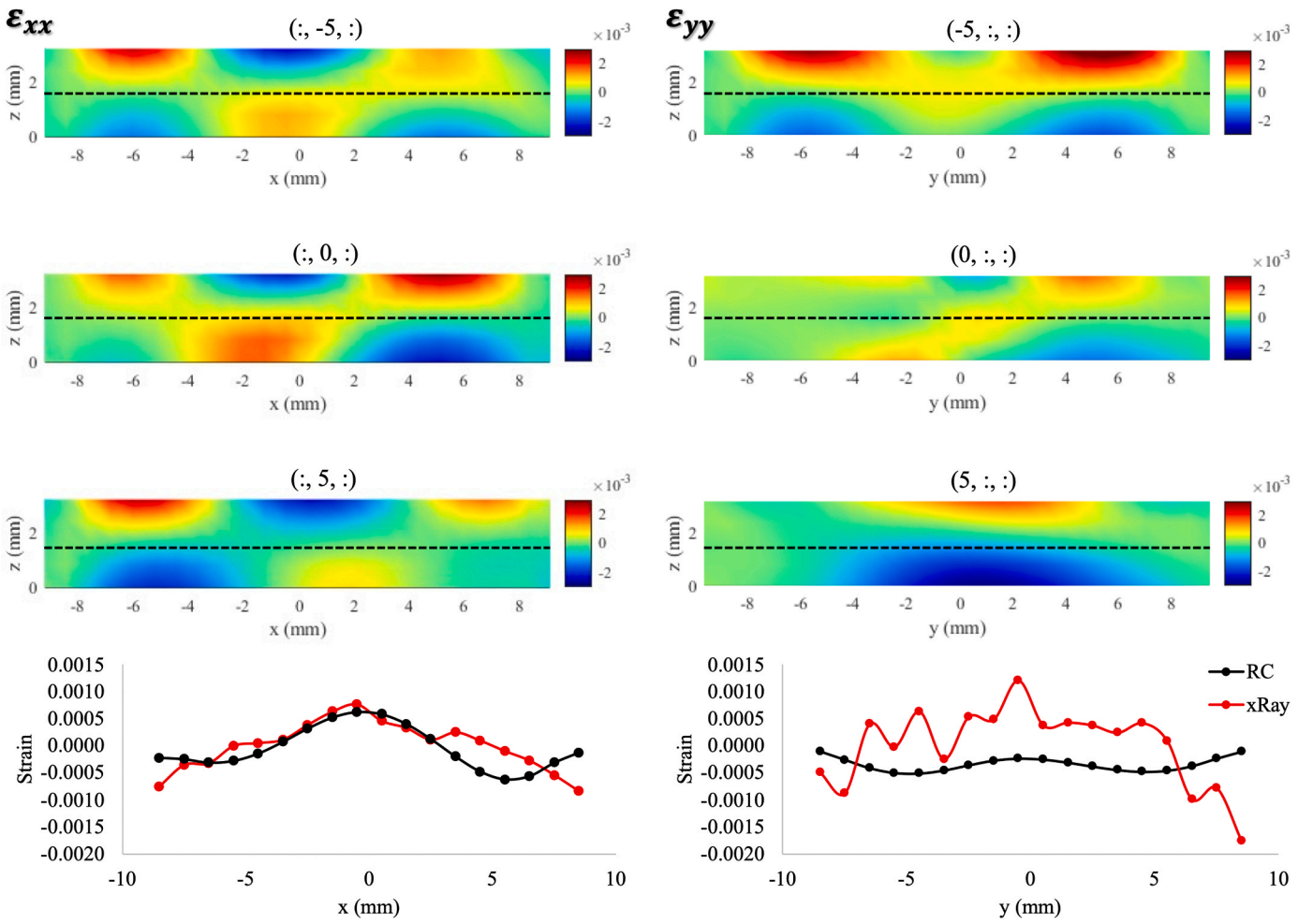


**Fig. 12.** Residual elastic strains quantified using diffraction beams distributed along the profile lines are compared with the planar distribution of xx- and yy-components of residual elastic strains calculated by the model at the planes where diffraction beams pass through.

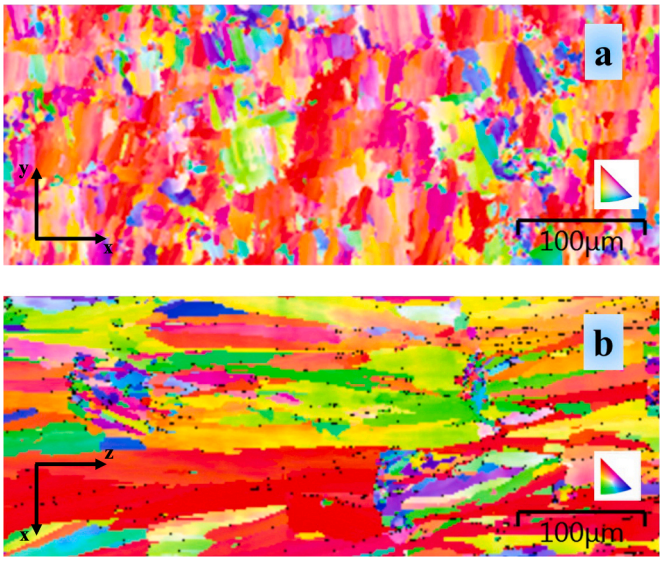


**Fig. 13.** EBSD images of (a) equiaxed grains from the top surface and (b) elongated grains from the side surface of the CM 247 LC part.

allows the quantification of residual elastic strains [80,81] using Eq. 1 where $\varepsilon_{\phi,\psi}$ is the strain positioned according to polar coordinates represented by angles $\phi$ and $\psi$, illustrated in Fig. 2, in terms of normal and shear strain components defined by $\varepsilon_{ij}$. i and j in this case are used to denote x-, y- and z-axes in cartesian coordinates namely by means of the X-ray diffraction $\sin^2\psi$ technique.

$$\varepsilon_{\phi,\psi} = \varepsilon_{xx}\ \cos^2\phi\sin^2\psi + \varepsilon_{xy}\sin2\phi\sin^2\psi + \varepsilon_{yy}\ \sin^2\phi\sin^2\psi + \varepsilon_{zz}\ \cos^2\psi + \varepsilon_{xz}\cos\phi\sin2\psi + \varepsilon_{yz}\sin\phi\sin2\psi \quad (1)$$

Strain components in Eq. (1) can be redefined in terms of stress components, $\sigma_{ij}$, using the compliance form of Hooke's Law given in Eq. 2 where E denotes Young's modulus, v represents Poisson's ratio, $\sigma_{kk}$ defines the sum of normal components of stress and $\delta_{ij}$ is the Kronecker delta.

$$\varepsilon_{ij} = \frac{1}{E}\left[(1+v)\sigma_{ij} - v\sigma_{kk}\delta_{ij}\right] \quad (2)$$

The revised form of Eq. (1) in terms of the stress components, Young's modulus and Poison's ratio is given in Eq. (3).

$$\varepsilon_{\phi,\psi} = \frac{1+v}{E}\left(\sigma_{xx}\ \cos^2\phi + \sigma_{xy}\sin2\phi + \sigma_{yy}\ \sin^2\phi - \sigma_{zz}\right)\sin^2\psi + \frac{1+v}{E}\sigma_{zz} \quad (3)$$

$$-\frac{v}{E}(\sigma_{xx}+\sigma_{yy}+\sigma_{zz})+\frac{1+v}{E}(\sigma_{xz}\cos\phi+\sigma_{yz}\sin\phi)\sin2\psi$$

In the case of determination of surface stresses using lattice spacing, the stress components normal to the surface, $\sigma_{xz}$, $\sigma_{yz}$ and $\sigma_{zz}$, are set to zero and strain components, $\varepsilon_{\phi,\psi}$ and $\varepsilon_{zz}$, are redefined in terms of lattice spacing for angles $\phi$ and $\psi$ as $d_{\phi,\psi}$ and for unstressed state as $d_0$ in Eq. (4).

$$\frac{d_{\phi,\psi}-d_0}{d_0}=\frac{1+v}{E}(\sigma_{xx}\ \cos^2\phi+\sigma_{xy}\sin2\phi+\sigma_{yy}\ \sin^2\phi-\sigma_{zz})\sin^2\psi+\frac{d_{\phi,\psi=0}-d_0}{d_0} \tag{4}$$

$$\sigma_\phi=\sigma_{xx}\ \cos^2\phi+\sigma_{xy}\sin2\phi+\sigma_{yy}\ \sin^2\phi-\sigma_{zz} \tag{5}$$

Rearranging strain terms in Eq. 4 by defining unstressed state as the lattice spacing of normal component of strain that is normal to surface when the angle $\psi$ is zero, $d_{\phi,\psi=0}$, and implementing stress component corresponding to the angle $\phi$ as expressed in Eq. (5), provided the liner relationship between the strain states corresponding to lattice spacings measured at different angles, $\psi$, and $\sin^2\psi$ given in Eq. (6).

$$\sigma_\phi=\frac{1+v}{E}\frac{1}{\sin^2\psi}\frac{d_{\phi,\psi}-d_{\phi,\psi=0}}{d_{\phi,\psi=0}} \tag{6}$$

The quantification of this linear relationship at each measurement point on the gridded top surface of CM 247 LC additive manufacturing part allows the calculation of normal components of planar residual stresses using Young's modulus and Poisson's ratio. The mapped residual stress components, $\sigma_{xx}$ and $\sigma_{yy}$, are averaged through the x- and y-axes and distributed along the y- and x-axes respectively as illustrated in Fig. 2 for comparing with averaged distribution of model calculations.

The X-ray $\sin^2\psi$ technique was practiced using lattice spacing measurements obtained at four angles, $\psi=[0.0, 15.0, 30.0, 45.0]$. Measurements were taken on the surface of before cut condition of the printed body using a beam size with dimensions of $100\times100$ μm. Lattice spacings for data from each measurement point at each angle was calculated using the GSAS-II Crystallography Data Analysis Software. Data set from each measurement point was analysed, by determining the slope of linear least squares fit between $\sin^2\psi$ and strain states corresponding to lattice spacings, and residual stresses are calculated using Eq. (6). The standard error of linear least squares analysis is also calculated for the determination of error range.

In 1998, Korsunsky et al. [82] introduced the use of synchrotron X-ray diffraction (XRD) for the two-dimensional mapping of strain distribution in materials with thick sampling volumes. The diffraction patterns recorded as digital images are evaluated for the lateral strain, $\varepsilon$, in any chosen direction according to the radial displacement by comparing the measured ring diameter with the reference condition using Eq. (7). Successful applications of this technique can be found in the papers that aim at quantifying residual stresses in the studies [83–85] performed after the initiation of this technique in 1998. This technique was used for the quantification of residual stresses averaged along the beam transmission path in CM 247 LC additive manufacturing part. The scans that penetrate along the x- and y-axes were used to create residual elastic stress maps over yz- and xy-planes, respectively. Calculation of residual elastic strains was achieved using the constitutive relation between stress and strain components defined by Hooke's Law given in Eq. (2) where $D_0$ and D denote the diameter of Debye-Scherrer rings belonging to reference stress free and target states of the material.

$$\varepsilon=\frac{D_0-D}{D_0} \tag{7}$$

Diffraction measurements for the determination of the radius of Debye-Scherrer rings were conducted in the as-printed condition of the printed body. The beams that travel through the material provided information about the average residual stress along the path. Scans were performed from two sides, which provided information about the distribution of the xx- and yy-components of residual stress along the x- and y-axes, respectively. Strain values were quantified using Eq. (7), and the diameter of Debye-Scherrer rings were determined by the caking method. The diameter of the reference stress-free condition is difficult to determine, as it was discussed in many other related studies cited in the Introduction section. Therefore, the diameter belonging to the reference stress free state was determined to be the average of all diameters calculated for all measurement points. For the comparison of experimental quantifications with the results of the voxel-based full-field eigenstrain reconstruction method, the calculations of the numerical model were averaged along the same path of the diffraction beam by interpolating residual stress values into the same volume occupied by the beam size with dimensions of $100\times100$ μm.

## 3. Results

The three-dimensional plots in Fig. 3 display the surface coordinate distribution measured using the optical microscope before and after the non-contact cutting process. The observed changes in the coordinates on the material's top surface are solely attributed to the relaxation of residual stresses formed during the PBF additive manufacturing of the body. The noisy distribution of z-coordinates in the profilometry data is due to the surface roughness of the printed body. Since hDIC relies on the correlation of the z-component of profilometry data, the noisy distribution caused by surface roughness was not subjected to any regression analysis.

The results of regression analysis of displacements, that were calculated by the hDIC using optical profilometry data performed using cubic polynomial functions, to capture main trends of the two-dimensional distribution of displacements are given in the left column of Fig. 4. The x-component of displacements, Dx, shows a variation along the x-axis while they have slight changes in the y-axis. Similarly, the y-component of displacements, Dy, have strong variation along the y-axis while they keep a stable form along the x-axis. These results show that the rectangular printed body has a concave shape after the non-contact cutting process. This claim has been proven by the distribution of the z-component of displacements, Dz, that shows the conversion into a concave form. Displacements calculated by the finite element method (FEniCS) based numerical model, which are given in the right column of Fig. 4, show an excellent match with the displacements calculated by the hDIC. This self-check property of the voxel-based eigenstrain reconstruction method provides the first validation in terms of displacements. However, this validation is not sufficient because the calculated displacements correspond to the top surface only, and there can be an infinite number of combination of eigenstrain states that may result in such a distribution of displacements. Therefore, in order to be satisfied with the reliability of full-field eigenstrain reconstruction, further validations were done using other reliable experimental techniques.

Line plots of six residual stress components are given in Fig. 5 along with the distribution of Von Mises yield criterion. Both shear and normal components of residual stresses seems to be shirked after cut. Shear stresses on the top surface along the red line have invisible magnitude while normal components have high magnitudes varying along the diagonal path. On the other hand, shear components have visible magnitudes along the diagonal blue path that distribute through the thickness and higher relaxation after separation from the base is observed in the regions closer to the top surface of the printed body.

The study of Alhuzaim et. al. [21] show that the tensile strength of CM 247 LC thin walls manufactured using direct laser deposition (DLD) technique has the potential to reach up to 1120 MPa, depending on the processing conditions. In the case of eigenstrain-based modelling, the resulting residual stresses are expected to be less than or equal to the tensile strength of the printed body, as the permanent plastic strains are mapped and imported according to the experimental data. The continuum model that solves the direct problem of eigenstrain is structured based on the assumption of isotropic distribution of material properties, but in a real printed body, it is less likely to obtain a homogeneous

distribution of tensile strength. On the other hand, eigenstrain-based modelling is structured on isotropic properties of elasticity, and the nature of this kind of modelling eliminates the need for isotropic distribution of plastic properties. Accordingly, the calculations of the presented model are free from limitations of plasticity, and the peak values of the von Mises criterion might reach the local limits of yield or tensile strength as illustrated in Fig. 5.

Line plots along the diagonal blue and red paths also show that the magnitudes of the normal components of residual stress are reduced after the separation from the base, but they continue to exist in a different form with high strength as illustrated in Fig. 5. The reason for this transformation is likely due to the bending of the planar printed body into a concave form. To investigate this claim, further analyses were performed on the planar distribution of the variation of the xx- and yy-components of residual stress along the yz- and xz-planes, respectively, passing through the origin. Fig. 6 shows the change in stress state after the separation of the part from the base. The magnitude of change in the xx- and yy-components of residual stress due to the separation shows a significant resemblance to the bending of plates. Both stress states have a linear variation along the height, with a distribution from compressive to tensile and a neutral state at around the centre. However, the chaotic nature of the PBF additive manufacturing process makes the classification of bending difficult.

According to the symmetric variation of the xx-component of residual stresses along the entire path of the x-axis, it can be stated that static equilibrium under the influence of the xx-component of residual stresses can be satisfied by corresponding bending moments. On the other hand, the influence of the lower magnitude of change in the y-component of displacements and related bending moments results in an asymmetric variation of the yy-component of residual stresses along the y-axis. Accordingly, it can be stated that, similar to the bending of plates, the displacements as a result of the relaxation of residual stresses create bending moments that are balanced by new forms of residual stresses to satisfy static equilibrium.

The results presented up to this point show that the voxel-based full-field eigenstrain reconstruction of residual stress provides valuable information for understanding the mechanics behind the complex deformations that occur due to manufacturing processes that have chaotic effects at micro and nano scales. The purpose of this study is to accurately map residual stresses with the help of limited experimental data. Therefore, a detailed view of the results of the reconstruction process is given in Fig. 7 in the form of transparent three-dimensional plots of the xx- and yy-components of residual stress. These illustrations show that the dominance of tensile stresses is replaced by compressive components with decreasing height in the before-cut condition. After the removal of the printed body from the base, the resulting stresses have lower magnitude and a visually more homogeneous distribution, but with variations due to the influence of bending moments as discussed before.

Detailed views of the distribution of xx- and yy-components of residual stress in the top, middle and bottom layers are illustrated, as contour plots for both before and after separation from the base, in Figs. 8, 9 and 10 respectively. These plots clearly present the symmetric nature of the distribution of residual stresses along the hight of the printed body. Distribution of residual stresses in the top layer seem have a twin with opposite sign in the bottom layer.

The contour plot of middle layer given in Fig. 9 presents the whole picture about neural state of residual stresses. As indicated in the case of bending moments, residual stresses in the middle layer do not change after the separation from the base. Although the bending of printed body cannot be classified as bending to a deployable surface or symmetric bending because of inhomogeneities in the distribution of residual stresses, it can be stated that mechanical effects of displacements due to stress relaxation after separation from the base can be explained by bending moments. This understanding is crucial because bending moments cause formation of new residual stress field that take place the stresses in the before cut condition.

The second validation of calculations of voxel-based full-field eigenstrain reconstruction method was achieved by the experimental quantification of planar distribution of xx- and yy-components of residual stresses. Residual stresses quantified by the X-ray diffraction $\sin^2\psi$ technique that were averaged through the x- and y-axes and distributed along the y- and x-axes respectively were compared with the averaged values of model calculations as illustrated in Fig. 11. The results show that there is a very good match between diffraction and model calculations of residual stresses. Even though the error range of experimental results is high, the overall trends of distribution of averaged values show excellent agreement, providing a good validation of the eigenstrain model by a highly reliable diffraction-based experimental technique.

The surface of the printed body was not treated before the experimental measurement of lattice spacing, and accordingly, diffraction measurements were performed on the as-printed surface. This caused the Debye-Scherrer rings to appear in a grainy form, but the Rietveld refinement technique combined with the caking method allowed reliable determination of the lattice spacings. The high standard error range can be a result of this grainy form of experimental data, but measurement in as-printed condition was compulsory in order to prevent creation of additional shear stress fields due to surface processing.

The third and final experimental validation of the voxel-based full-field eigenstrain reconstruction method was achieved by using high-flux diffraction beams that penetrated all the way through the x- and y-axes normal to the y- and x-axes, respectively. The comparison between residual elastic strain quantifications from high flux transmission diffraction beam data and numerical model calculations is shown in Fig. 12 to understand the changes in stress state based on the underlying facts about bending of plates [86]. The left column of the figure shows the xx-component, while the right column shows the yy-component of residual elastic strains. In addition to the comparison between the model and experimental results, the distribution of residual elastic strains on the planes that the diffraction beam penetrates is also shown. The planes are located at the origin and $\pm$ 5 mm away from the origin.

The quantifications of the xx-component of residual elastic strain show a very good match between the voxel-based eigenstrain reconstruction method and the high flux transmission diffraction beam data. This provides evidence of the high reliability of the voxel-based eigenstrain reconstruction method. However, the model calculations and diffraction-based quantifications of the yy-component of residual stress in the middle plane do not show a good match. This deviation is likely due to experimental errors caused by the cutting plan. In the cutting process, the EDM arc elongates along the x-axis while it travels along the y-axis. This cutting plan produces a homogeneous elastic response due to the non-contact separation of the printed part along the x-axis, while the response is gradual along the y-axis.

Even though the diffraction-based quantifications on the top surface of the part show a good match with the yy-component of residual elastic strain calculations from the voxel-based eigenstrain reconstruction method, the in-volume measurements do not show a similar match along one of the axes. This is because the high flux transmission diffraction beams used for the in-volume measurements were penetrated away from the source of experimental data, which magnified the errors caused by the cutting process. This phenomenon needs to be investigated further by testing different cutting plans and validating the results with diffraction-based experimental residual elastic strain quantifications. However, this is beyond the scope of this study.

During the manufacturing of CM 247 LC additive manufacturing part, nucleation is expected to initiate grain formation at the solid base and molten liquid metal interface. Complex rapid heating and cooling cycles repeated during the PBF process induce heterogeneous nucleation as homogeneous nucleation requires these cycles to be expanded into large time scales. Grains elongate along the building direction while having an equiaxed form parallel to the building plane. The characteristic form of grains belonging to the PBF additive manufacturing process was analysed using electron backscattered (EBSD) images illustrated in

Fig. 13. The microstructure map in the top image belongs to the section surface normal to the build direction (z-axis) and the bottom map is for the section surface normal to the y-axis. Results show that CM 247 LC part accommodates this characteristic microstructure that supports the reliability of production of this part.

## 4. Conclusion

The voxel-based eigenstrain reconstruction method has previously demonstrated its success in numerical experiments, achieving highly accurate reconstruction of eigenstrains and residual stresses with minimal triaxial displacement data. This study extends this analysis to real case experiments, utilizing data processed by hDIC. Monochromatic diffraction was also used to quantify residual stresses in the printed body before separation from the base for achieving validation along with the validation of the experimentally determined displacements in the post-separation state against those calculated during reconstruction. These validations underscore the capability of eigenstrain-based modelling to determine residual stress after various processing conditions without process modelling.

Residual stresses in additive manufacturing parts represent a critical and often complex aspect of the manufacturing process and have a significant impact on the structural integrity, dimensional accuracy, and overall performance of additive manufacturing parts. Therefore, achieving cost-effective prediction of residual stress fields is essential for designing components with minimized residual stress. The integration of the hDIC technique with the voxel-based eigenstrain reconstruction method has been proven to be effective in volumetric mapping of residual stresses in additive manufacturing parts based on cost-effective optical profilometry measurements. Volumetric analysis achieved by this approach allows the determination of unpredictable residual stress hotspots formed due to the discontinuous processing conditions of this manufacturing process that cannot be achieved by currently available process modelling and experimentation techniques.

## CRediT authorship contribution statement

**Fatih Uzun:** Visualization, Validation, Software, Resources, Methodology, Investigation, Funding acquisition, Formal analysis, Data curation, Conceptualization, Writing - original draft, Writing - review & editing. **Hector Basoalto:** Investigation. **Konstantinos Liogas:** Investigation. **Jingwei Chen:** Investigation. **Igor P.Dolbnya:** Investigation. **Zifan Ivan Wang:** Investigation. **Alexander M. Korsunsky:** Supervision, Project administration, Methodology, Funding acquisition, Conceptualization.

## Declaration of Competing Interest

The authors declare that they have no known competing financial interests or personal relationships that could have appeared to influence the work reported in this paper.

## Data Availability

Data will be made available on request.

## Acknowledgements

The authors acknowledge EuroHPC project grant EHPC-DEV-2022D10-054 for allowing the simulations to be performed on the Luxembourg national supercomputer MeluXina and are also grateful to LuxProvide teams for their expert support. The authors thank Diamond Light Source (Didcot, UK) for beamtime allocations MM30460-1 and MG31917-1 to B16 and I12 beamlines, respectively.

## References

[1] R.J. Smith, G.J. Lewis, D.H. Yates, Development and application of nickel alloys in aerospace engineering, Aircr. Eng. Aerosp. Technol. 73 (2001) 138–146, https://doi.org/10.1108/00022660110694995.
[2] M. Valenti, Building more efficient turbines, Mech. Eng. 116 (1994) 52–56.
[3] J.R. Davis, A.S.M.I.H. Committee. Nickel, Cobalt, and Their Alloys, ASM International, 2000.
[4] J.H. Boswell, D. Clark, W. Li, M.M. Attallah, Cracking during thermal post-processing of laser powder bed fabricated CM247LC Ni-superalloy, Mater. Des. 174 (2019), 107793, https://doi.org/10.1016/j.matdes.2019.107793.
[5] I.A. Choudhury, M.A. El-Baradie, Machinability of nickel-base super alloys: a general review, J. Mater. Process Technol. 300 (1998) 278–284, https://doi.org/10.1016/s0924-0136(97)00429-9.
[6] E.O. Ezugwu, Z.M. Wang, A.R. Machado, The machinability of nickel-based alloys: a review, J. Mater. Process Technol. 86 (1998) 1–16, https://doi.org/10.1016/S0924-0136(98)00314-8.
[7] S. Sanchez, P. Smith, Z. Xu, G. Gaspard, C.J. Hyde, W.W. Wits, I.A. Ashcroft, H. Chen, A.T. Clare, Powder Bed Fusion of nickel-based superalloys: a review, Int J. Mach. Tools Manuf. 165 (2021), https://doi.org/10.1016/j.ijmachtools.2021.103729.
[8] I. Yadroitsev, I. Shishkovsky, P. Bertrand, I. Smurov, Manufacturing of fine-structured 3D porous filter elements by selective laser melting, Appl. Surf. Sci. 255 (2009) 5523–5527, https://doi.org/10.1016/j.apsusc.2008.07.154.
[9] W. Danesi, R. Thielemann, Nickel Base Alloy 3720509 (1970).
[10] R.S.K. Harris, G. Erickson, MAR M 247 Derivations - CM 247 LC DS Alloy and CMSX Single Crystal Alloys: Properties & Performance, in: J.F.R. M. Gell, C. S. Kortovich, R. H. Bricknell, W. B. Kent (Ed.), Fifth International Symposium on Superalloys, The Metallurgical Society of AIME, Champion, Pennsylvania, USA, 1984: pp. 221–230. https://doi.org/10.7449/1984/SUPERALLOYS_1984_221_230.
[11] G.L. Erickson, K. Harris, R.E. Schwer, Ds Cm 247 Lc - characteristic properties with optimized solutioning, Techniques (1984) 401–417.
[12] G.L. Erickson, K. Harris, R.E. Schwer, Directionally Solidified DS CM 247 LC - Optimized Mechanical Properties Resulting From Extensive γ′ Solutioning, in: Proceedings of the ASME 1985 International Gas Turbine Conference and Exhibit. Volume 4: Manufacturing Materials and Metallurgy; Ceramics; Structures and Dynamics; Controls, Diagnostics and Instrumentation; Education; Process Industries, ASME, Houston, Texas, USA, 1985. https://doi.org/10.1115/85-GT-107.
[13] A. Seidel, T. Finaske, A. Straubel, H. Wendrock, T. Maiwald, M. Riede, E. Lopez, F. Brueckner, C. Leyens, Additive manufacturing of powdery Ni-based superalloys Mar-M-247 and CM 247 LC in hybrid laser metal deposition, Met. Mater. Trans. A Phys. Met. Mater. Sci. 49 (2018) 3812–3830, https://doi.org/10.1007/s11661-018-4777-y.
[14] M.B. Henderson, D. Arrell, M. Heobel, R. Larsson, G. Marchant, Nickel-based superalloy welding practices for industrial gas turbine applications, Sci. Technol. Weld. Join. 9 (2004) 1–14, https://doi.org/10.1179/136217104225017099.
[15] M.J. Donachie, S.J. Donachie, Superalloys: A Technical Guide, in: 2002.
[16] O.A. Ojo, N.L. Richards, M.C. Chaturvedi, Contribution of constitutional liquation of gamma prime precipitate to weld HAZ cracking of cast Inconel 738 superalloy, Scr. Mater. 50 (2004) 641–646, https://doi.org/10.1016/j.scriptamat.2003.11.025.
[17] S. Catchpole-Smith, N. Aboulkhair, L. Parry, C. Tuck, I.A. Ashcroft, A. Clare, Fractal scan strategies for selective laser melting of 'unweldable' nickel superalloys, Addit. Manuf. 15 (2017) 113–122, https://doi.org/10.1016/j.addma.2017.02.002.
[18] R. Engeli, T. Etter, S. Hövel, K. Wegener, Processability of different IN738LC powder batches by selective laser melting, J. Mater. Process Technol. 229 (2016) 484–491, https://doi.org/10.1016/j.jmatprotec.2015.09.046.
[19] D.D. Gu, W. Meiners, K. Wissenbach, R. Poprawe, Laser additive manufacturing of metallic components: Materials, processes and mechanisms, Int. Mater. Rev. 57 (2012) 133–164, https://doi.org/10.1179/1743280411Y.0000000014.
[20] L.N. Carter, M.M. Attallah, R.C. Reed, Laser powder bed fabrication of nickel-base superalloys: Influence of parameters; characterisation, quantification and mitigation of cracking, Proc. Int. Symp. . Superalloys (2012) 577–586, https://doi.org/10.7449/2012/superalloys_2012_577_586.
[21] A. Alhuzaim, S. Imbrogno, M.M. Attallah, Direct laser deposition of crack-free CM247LC thin walls: mechanical properties and microstructural effects of heat treatment, Mater. Des. 211 (2021), 110123, https://doi.org/10.1016/J.MATDES.2021.110123.
[22] J. Yang, F. Li, Z. Wang, X. Zeng, Cracking behavior and control of Rene 104 superalloy produced by direct laser fabrication, J. Mater. Process Technol. 225 (2015) 229–239, https://doi.org/10.1016/j.jmatprotec.2015.06.002.
[23] J. Xu, Y. Ding, Y. Gao, H. Wang, Y. Hu, D. Zhang, Grain refinement and crack inhibition of hard-to-weld Inconel 738 alloy by altering the scanning strategy during selective laser melting, Mater. Des. 209 (2021), 109940, https://doi.org/10.1016/j.matdes.2021.109940.
[24] M. Cloots, P.J. Uggowitzer, K. Wegener, Investigations on the microstructure and crack formation of IN738LC samples processed by selective laser melting using Gaussian and doughnut profiles, Mater. Des. 89 (2016) 770–784, https://doi.org/10.1016/j.matdes.2015.10.027.
[25] M. Zhong, H. Sun, W. Liu, X. Zhu, J. He, Boundary liquation and interface cracking characterization in laser deposition of Inconel 738 on directionally solidified Ni-based superalloy, Scr. Mater. 53 (2005) 159–164, https://doi.org/10.1016/j.scriptamat.2005.03.047.
[26] H. Wang, L. Chen, B. Dovgyy, W. Xu, A. Sha, X. Li, H. Tang, Y. Liu, H. Wu, M. S. Pham, Micro-cracking, microstructure and mechanical properties of Hastelloy-X

alloy printed by laser powder bed fusion: As-built, annealed and hot-isostatic pressed, Addit. Manuf. 39 (2021), 101853, https://doi.org/10.1016/j.addma.2021.101853.
[27] J. Mathar, Determination of initial stresses by measuring the deformations around drilled holes, Trans. ASME 56 (1934) 249–254.
[28] F. Stablein, Spannungsmessungen in einseitig abgeloschten Knuppeln, Kruppsch Mon. 12 (1931) 93–99.
[29] S. Vaidyanathan, I. Finnie, Determination of residual stresses from stress intensity factor measurements, (1971).
[30] M.B. Prime, The Contour Method - Simple 2-D Mapping of Residual Stresses, (2000) 121–127. https://doi.org/10.1115/IMECE2000–1262.
[31] M. Kartal, M. Turski, G. Johnson, M.E. Fitzpatrick, S. Gungor, P.J. Withers, L. Edwards, Residual stress measurements in single and multi-pass groove weld specimens using neutron diffraction and the contour method, Mater. Sci. Forum 524–525 (2006) 671–676, https://doi.org/10.4028/www.scientific.net/MSF.524-525.671.
[32] M.E. Kartal, Y.H. Kang, A.M. Korsunsky, A.C.F.F. Cocks, J.P. Bouchard, The influence of welding procedure and plate geometry on residual stresses in thick components, Int J. Solids Struct. 80 (2016) 420–429, https://doi.org/10.1016/j.ijsolstr.2015.10.001.
[33] F. Hosseinzadeh, J. Kowal, P.J. Bouchard, Towards good practice guidelines for the contour method of residual stress measurement, J. Eng. (2014), https://doi.org/10.1049/joe.2014.0134.
[34] M. Turski, L. Edwards, Residual stress measurement of a 316l stainless steel bead-on-plate specimen utilising the contour method, Int. J. Press. Vessels Pip. 86 (2009) 126–131, https://doi.org/10.1016/j.ijpvp.2008.11.020.
[35] A. Tognan, L. Laurenti, E. Salvati, Contour method with uncertainty quantification: a robust and optimised framework via gaussian process regression, Exp. Mech. 62 (2022) 1305–1317, https://doi.org/10.1007/s11340-022-00842-w.
[36] W.L. Bragg, The diffraction of short electromagnetic Waves by a Crystal, Scientia 23 (1929).
[37] M.C. Smith, A.C. Smith, C. Ohms, R.C. Wimpory, The NeT Task Group 4 residual stress measurement and analysis round robin T on a three-pass slot-welded plate specimen, Int. J. Press. Vessels Pip. 164 (2018) 3–21, https://doi.org/10.1016/j.ijpvp.2017.09.003.
[38] M.C. Smith, A.C. Smith, R. Wimpory, C. Ohms, A review of the NeT Task Group 1 residual stress measurement and analysis round robin on a single weld bead-on-plate specimen, Int. J. Press. Vessels Pip. 120– 121 (2014) 93–140, https://doi.org/10.1016/j.ijpvp.2014.05.002.
[39] D.S. Hughes, J.L. Kelly, Second-order elastic deformation of solids, Phys. Rev. 92 (1953) 1145–1149, https://doi.org/10.1103/PhysRev.92.1145.
[40] F. Uzun, A.N. Bilge, Ultrasonic investigation of the effect of carbon content in carbon steels on bulk residual stress, J. Nondestr Eval. 34 (2015), https://doi.org/10.1007/s10921-015-0284-x.
[41] C.V. Raman, K.S. Krishnan, A new type of secondary radiation, Nature 121 (1928) 501–502, https://doi.org/10.1038/121501c0.
[42] J. Everaerts, E. Salvati, F. Uzun, L. Romano Brandt, H. Zhang, A.M. Korsunsky, Separating macro- (Type I) and micro- (Type II+III) residual stresses by ring-core FIB-DIC milling and eigenstrain modelling of a plastically bent titanium alloy bar, Acta Mater. 156 (2018) 43–51, https://doi.org/10.1016/j.actamat.2018.06.035.
[43] A.M. Korsunsky, M. Sebastiani, E. Bemporad, Focused ion beam ring drilling for residual stress evaluation, Mater. Lett. 63 (2009) 1961–1963, https://doi.org/10.1016/j.matlet.2009.06.020.
[44] A.J.G. Lunt, A.M. Korsunsky, A review of micro-scale focused ion beam milling and digital image correlation analysis for residual stress evaluation and error estimation, Surf. Coat. Technol. 283 (2015) 373–388, https://doi.org/10.1016/j.surfcoat.2015.10.049.
[45] E. Salvati, A.J.G. Lunt, S. Ying, T. Sui, H.J. Zhang, C. Heason, G. Baxter, A. M. Korsunsky, Eigenstrain reconstruction of residual strains in an additively manufactured and shot peened nickel superalloy compressor blade, Comput. Methods Appl. Mech. Eng. 320 (2017) 335–351, https://doi.org/10.1016/j.cma.2017.03.005.
[46] Z. Wang, E. Denlinger, P. Michaleris, A.D. Stoica, D. Ma, A.M. Beese, Residual stress mapping in Inconel 625 fabricated through additive manufacturing: method for neutron diffraction measurements to validate thermomechanical model predictions, Mater. Des. 113 (2017) 169–177, https://doi.org/10.1016/j.matdes.2016.10.003.
[47] D.W. Brown, J.D. Bernardin, J.S. Carpenter, B. Clausen, D. Spernjak, J. M. Thompson, Neutron diffraction measurements of residual stress in additively manufactured stainless steel, Mater. Sci. Eng. A 678 (2016) 291–298, https://doi.org/10.1016/j.msea.2016.09.086.
[48] C. Ohms, R.C. Wimpory, D.E. Katsareas, A.G. Youtsos, NET TG1: residual stress assessment by neutron diffraction and finite element modeling on a single bead weld on a steel plate, Int. J. Press. Vessels Pip. 86 (2009) 63–72, https://doi.org/10.1016/j.ijpvp.2008.11.009.
[49] M. Hofmann, R.C. Wimpory, NET TG1: Residual stress analysis on a single bead weld on a steel plate using neutron diffraction at the new engineering instrument “STRESS-SPEC, Int. J. Press. Vessels Pip. 86 (2009) 122–125, https://doi.org/10.1016/j.ijpvp.2008.11.007.
[50] S. Pratihar, M. Turski, L. Edwards, P.J. Bouchard, Neutron diffraction residual stress measurements in a 316L stainless steel bead-on-plate weld specimen, Int. J. Press. Vessels Pip. 86 (2009) 13–19, https://doi.org/10.1016/j.ijpvp.2008.11.010.
[51] R.C. Wimpory, C. Ohms, M. Hofmann, R. Schneider, A.G. Youtsos, Statistical analysis of residual stress determinations using neutron diffraction, Int. J. Press. Vessels Pip. 86 (2009) 48–62, https://doi.org/10.1016/j.ijpvp.2008.11.003.
[52] Y. Ueda, T. Yamakawa, Analysis of thermal elastic-plastic stress and strain during welding by finite element method, Jpn. Weld. Soc. Trans. 2 (1971).
[53] X. Shan, C.M. Davies, T. Wangsdan, N.P. O’Dowd, K.M. Nikbin, Thermo-mechanical modelling of a single-bead-on-plate weld using the finite element method, Int. J. Press. Vessels Pip. 86 (2009) 110–121, https://doi.org/10.1016/j.ijpvp.2008.11.005.
[54] C.J. Hamelin, O. Muránsky, M.C. Smith, T.M. Holden, V. Luzin, P.J. Bendeich, L. Edwards, C.J. Hamelin, O. Mura, V. Luzin, P.J. Bendeich, L. Edwards, Validation of a numerical model used to predict phase distribution and residual stress in ferritic steel weldments, Acta Mater. 75 (2014) 1–19, https://doi.org/10.1016/j.actamat.2014.04.045.
[55] C.E. Truman, M.C. Smith, The NeT residual stress measurement and modelling round robin on a single weld bead-on-plate specimen, Int. J. Press. Vessels Pip. 86 (2009) 1–2, https://doi.org/10.1016/j.ijpvp.2008.11.018.
[56] T. Mura, Micromechanics of Defects in Solids, Springer Netherlands, Dordrecht, 1987.
[57] A.M. Korsunsky, A. Teaching Essay on Residual Stresses and Eigenstrains, Butterworth-Heinemann, Oxford, United Kingdom, 2017.
[58] F. Uzun, A.M. Korsunsky, On the identification of eigenstrain sources of welding residual stress in bead-on-plate inconel 740H specimens, Int. J. Mech. Sci. 145 (2018) 231–245, https://doi.org/10.1016/j.ijmecsci.2018.07.007.
[59] F. Uzun, J. Everaerts, L.R. Brandt, M. Kartal, E. Salvati, A.M. Korsunsky, The inclusion of short-transverse displacements in the eigenstrain reconstruction of residual stress and distortion in in740h weldments, J. Manuf. Process 36 (2018) 601–612, https://doi.org/10.1016/j.jmapro.2018.10.047.
[60] F. Uzun, A.M. Korsunsky, On the application of principles of artificial intelligence for eigenstrain reconstruction of volumetric residual stresses in non-uniform Inconel alloy 740H weldments, Finite Elem. Anal. Des. 155 (2019) 43–51, https://doi.org/10.1016/j.finel.2018.11.004.
[61] F. Uzun, A.M. Korsunsky, On the analysis of post weld heat treatment residual stress relaxation in Inconel alloy 740H by combining the principles of artificial intelligence with the eigenstrain theory, Mater. Sci. Eng. A 752 (2019) 180–191, https://doi.org/10.1016/j.finel.2018.11.004.
[62] F. Uzun, C. Papadaki, Z. Wang, A.M. Korsunsky, Neutron strain scanning for experimental validation of the artificial intelligence based eigenstrain contour method, Mech. Mater. 143 (2020), 103316, https://doi.org/10.1016/j.mechmat.2020.103316.
[63] A.T. DeWald, M.R. Hill, Multi-axial contour method for mapping residual stresses in continuously processed bodies, Exp. Mech. 46 (2006) 473–490, https://doi.org/10.1007/s11340-006-8446-5.
[64] F. Uzun, A.M. Korsunsky, Voxel-based full-field eigenstrain reconstruction of residual stresses, Adv. Eng. Mater. (2023), https://doi.org/10.1002/adem.202201502.
[65] E. Arabul, A.J.G. Lunt, A. Novel Low-Cost DIC-Based Residual Stress Measurement, Device, Appl. Sci. 7233 (2022), https://doi.org/10.3390/app12147233.
[66] G.S. Schajer, B. Winiarski, P.J. Withers, Hole-drilling residual stress measurement with artifact correction using full-field DIC, in: C.E. Ventura, W.C. Crone, C. Furlong (Eds.), Experimental and Applied Mechanics, Volume 4, Springer, New York, New York, NY, 2013, pp. 403–414.
[67] D.V. Nelson, Residual stress determination using full-field optical methods, J. Phys.: Photonics 3 (2021), 044003, https://doi.org/10.1088/2515-7647/ac1ceb.
[68] M. Sutton, C. Mingqi, W. Peters, Y. Chao, S. McNeill, Application of an optimized digital correlation method to planar deformation analysis, Image Vis. Comput. 4 (1986) 143–150, https://doi.org/10.1016/0262-8856(86)90057-0.
[69] Z. Sun, J.S. Lyons, S.R. McNeill, Measuring microscopic deformations with digital image correlation, Opt. Lasers Eng. 27 (1997) 409–428, https://doi.org/10.1016/S0143-8166(96)00041-3.
[70] M. Luo, Displacement/strain measurements using an optical microscope and digital image correlation, Opt. Eng. 45 (2006), 033605, https://doi.org/10.1117/1.2182108.
[71] X. Li, W. Xu, M.A. Sutton, M. Mello, Nanoscale deformation and cracking studies of advanced metal evaporated magnetic tapes using atomic force microscopy and digital image correlation techniques, Mater. Sci. Technol. 22 (2006) 835–844, https://doi.org/10.1179/174328406×101283.
[72] Y. Sun, J.H.L. Pang, W. Fan, Nanoscale deformation measurement of microscale interconnection assemblies by a digital image correlation technique, Nanotechnology 18 (2007), https://doi.org/10.1088/0957-4484/18/39/395504.
[73] Z.H. Xu, M.A. Sutton, X. Li, Mapping nanoscale wear field by combined atomic force microscopy and digital image correlation techniques, Acta Mater. 56 (2008) 6304–6309, https://doi.org/10.1016/j.actamat.2008.08.044.
[74] F. Uzun, A.M. Korsunsky, The height digital image correlation (hDIC) technique for the identification of triaxial surface deformations, Int J. Mech. Sci. 159 (2019) 417–423, https://doi.org/10.1016/j.ijmecsci.2019.06.014.
[75] F. Uzun, A.M. Korsunsky, The use of surface topography for the identification of discontinuous displacements due to cracks, Metals 10 (2020) 1–13, https://doi.org/10.3390/met10081037.
[76] S. Dave, X. Song, F. Hofmann, K. Dragnevski, A.M. Korsunsky, Digital image correlation and finite element analysis of inter- and intra-granular deformation, Procedia Eng. 1 (2009) 197–200, https://doi.org/10.1016/j.proeng.2009.06.046.
[77] F. Uzun, A.I. Salimon, E.S. Statnik, C. Besnard, J. Chen, T. Moxham, E. Salvati, Z. Wang, A.M. Korsunsky, Polar transformation of 2D X-ray diffraction patterns and the experimental validation of the hDIC technique, Measurement 151 (2019), 107193, https://doi.org/10.1016/j.measurement.2019.107193.

[78] P. Zhou, Subpixel displacement and deformation gradient measurement using digital image/speckle correlation (DISC, Opt. Eng. 40 (2001) 1613, https://doi.org/10.1117/1.1387992.
[79] A.M. Korsunsky, L.R. Brandt, The effect of deposition parameters on the mechanical and transport properties in nanostructured Cu/W multilayer coatings, in: Functional Thin Films Technology, CRC Press, 2021, pp. 287–318.
[80] H.H. Lester, R.H. Aborn, Behaviour under stress of iron crystal in steel, Army Ordnance 6 (1925) 120–127.
[81] A.M. Korsunsky, A critical discussion of the sin2 ψ stress measurement technique, Mater. Sci. Forum 571– 572 (2008) 219–224, https://doi.org/10.4028/www.scientific.net/msf.571-572.219.
[82] A.M. Korsunsky, K.E. Wells, P.J. Withers, Mapping two-dimensional state of strain using synchroton X-ray diffraction, Scr. Mater. 39 (1998) 1705–1712, https://doi.org/10.1016/S1359-6462(98)00385-6.
[83] P.J. Withers, M. Preuss, P.J. Webster, D.J. Hughes, A.M. Korsunsky, Residual strain measurement by synchrotron diffraction, Mater. Sci. Forum 404– 407 (2002) 1–12, https://doi.org/10.4028/www.scientific.net/msf.404-407.1.
[84] T. Sui, I.A. Sandholzer, I. Baimpas, I.P. Dolbnya, A.D. Walmsley, P.J. Lumley, G. Landini, A.M. Korsunsky, Multiscale modelling and diffraction-based characterization of elastic behaviour of human dentine, Acta Biomater. 9 (2013) 7937–7947, https://doi.org/10.1016/j.actbio.2013.04.020.
[85] A.M. Korsunsky, X. Song, F. Hofmann, B. Abbey, M. Xie, T. Connolley, C. Reinhard, R.C. Atwood, L. Connor, M. Drakopoulos, Polycrystal deformation analysis by high energy synchrotron X-ray diffraction on the I12 JEEP beamline at Diamond Light Source, Mater. Lett. 64 (2010) 1724–1727, https://doi.org/10.1016/j.matlet.2010.04.023.
[86] S. Timoshenko, Theory of Plates and Shells, second ed., McGraw-Hill Book Company,, 1989.